Shock Waves
DOI 10.1007/s00193-015-0615-y

ORIGINAL ARTICLE

Interaction theory of hypersonic laminar near-wake flow behind an adiabatic circular cylinder

W. Schuyler Hinman[1] · **C. T. Johansen**[1]

Received: 16 June 2015 / Revised: 15 September 2015 / Accepted: 10 December 2015

Abstract The separation and shock wave formation on the aft-body of a hypersonic adiabatic circular cylinder were studied numerically using the open source software OpenFOAM. The simulations of laminar flow were performed over a range of Reynolds numbers ($8 \times 10^3 < Re < 8 \times 10^4$) at a free-stream Mach number of 5.9. Off-body viscous forces were isolated by controlling the wall boundary condition. It was observed that the off-body viscous forces play a dominant role compared to the boundary layer in displacement of the interaction onset in response to a change in Reynolds number. A modified free-interaction equation and correlation parameter has been presented which accounts for wall curvature effects on the interaction. The free-interaction equation was manipulated to isolate the contribution of the viscous–inviscid interaction to the overall pressure rise and shock formation. Using these equations coupled with high-quality simulation data, the underlying mechanisms resulting in Reynolds number dependence of the lip-shock formation were investigated. A constant value for the interaction parameter representing the part of the pressure rise due to viscous–inviscid interaction has been observed at separation over a wide range of Reynolds numbers. The effect of curvature has been shown to be the primary contributor to the Reynolds number dependence of the free-interaction mechanism at separation. The observations in this work have been discussed here to create a thorough analysis of the Reynolds number-dependent nature of the lip-shock.

Keywords Interaction theory · Hypersonic laminar near-wake · Computational fluid dynamics · Lip separation shock · Viscous–inviscid interaction

1 Introduction

Flow separation and the near-wake structure behind blunt bodies at hypersonic speeds have application primarily to re-entry vehicle aerodynamics and ballistics. In recent years, the fluid mechanics of hypersonic blunt body near-wakes have become of interest because of planetary entry vehicle development for past and current Mars exploration missions [14,19,25,27,28,33]. These flows have been investigated experimentally and numerically. However, these investigations have not focused on fundamental fluid mechanics and were largely capsule specific. Many more general investigations have been performed experimentally [13,18,24,30,32,38,43], numerically and analytically [6–9,12,15,17,21,26,31,36,40–42,44–47] for flows relevant to the laminar near-wake problem. A significant dependence on Reynolds number of the pertinent flow features is known. For example, Dewey [18] showed that for both a cylinder, and a wedge, base pressure had a clear dependence on Reynolds number. It was shown by Hama [24], using various boat-tail geometries, that the lip separation shock wave is primarily a viscous phenomenon regardless of the aft-body geometry. McCarthy and Kubota [32] showed that pressure distribution of a circular cylinder at Mach 6 was Reynolds number dependent. Park et al. [38], collected pressure data for a wide range of Reynolds numbers and showed a predictable dependence of the pressure minimum location based on Reynolds number. While the flow topology of the near-wake base flow problem is well observed, the understanding of the underlying Reynolds number-dependent mechanisms can still be improved. A gap

Communicated by H. Olivier.

✉ W. Schuyler Hinman
wshinman@ucalgary.ca

[1] 2500 University Dr. NW, Calgary, AB, Canada

Published online: 30 December 2015

in knowledge exists due to the limited resources and capabilities in the early work, and a lack of generality in modern investigations. A logical next step in this field of study is to use high-quality computational fluid dynamics (CFD) to study the near wake of a simplified geometry. The mechanism at separation can be analyzed through comparison to other problems featuring strong viscous–inviscid interaction such as shock wave boundary layer interactions. With modern computing power, a parametric analysis of the near-wake fluid mechanics using the full compressible Navier–Stokes equations is feasible. In the present work, the problem is studied through a series of CFD simulations of hypersonic flow over an adiabatic circular cylinder in two dimensions. The data gained from this CFD study will be used to improve basic mathematical descriptions of separation and lip shock formation. While some recent parametric studies exist [22,35,38], to the best knowledge of the authors, such a parametric study of the viscous–inviscid interaction in this flow problem has never been performed.

The laminar near-wake flow topology and the viscous–inviscid interactions referred to in this paper are shown in Fig. 1. Viscous–inviscid interaction phenomena occur on the body and in the wake, and are fundamental to understanding this flow problem. In the present work, the terms *weak* and *strong* interactions are used to distinguish between viscous–inviscid interactions where separation does not occur, and those that lead to separation and involve significant upstream influence, respectively. On the aft-body, a strong interaction leads to the formation of the lip separation shock. The reattachment shock is created by a similar mechanism that occurs at the wake reattachment point. Upstream of the wake, a weak interaction occurs on the body that alters the pressure distribution and the boundary layer properties. These mechanisms and their dependence on Reynolds number are the primary motivation for this work.

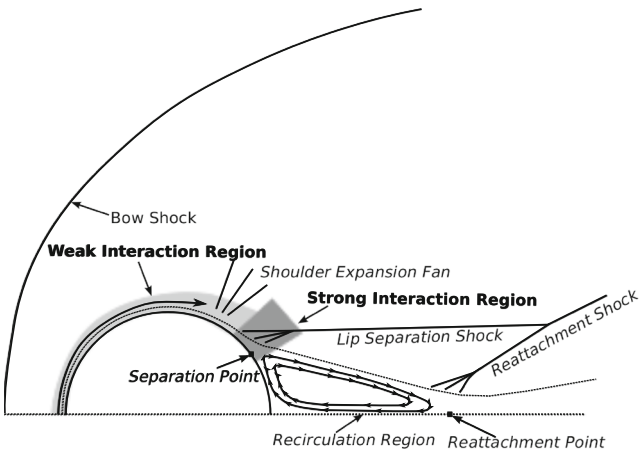

Fig. 1 Near-wake flow topology

Part of the present work is the incorporation of simulations with the no-slip boundary condition removed at the wall. The boundary condition in these cases only enforces flow tangency and does not produce a boundary layer. These simulations are referred to from herein as *slip simulations* (this is not meant to indicate any analogy to high Knudsen number or slip regime flow). In the slip simulations, the effect of viscosity is still present and therefore Reynolds number can still be manipulated. It is known that in some cases a separated region can be created in the absence of a boundary layer due to the presence of shock waves. By doing this here, the effects of viscous forces in the free shear layer and the effects of viscous forces in the boundary layer can be isolated. Through comparison of these results with the fully viscous simulations the relative importance of the off-body viscous effects and the boundary layer can be examined. Using this approach, the Reynolds number dependence of the separation interaction onset is to be studied. It is known that the location of the pressure minimum and thus the apparent onset of the interaction is dependent on Reynolds number. This is a combined effect of the incoming boundary layer and the viscous mechanisms of compression in the near-wake. Slip simulations remove one of these variable elements from the flow and thus allow their respective relative importance to be heuristically shown.

2 Free-interaction theory

In typical shock wave boundary layer interactions that lead to separation, the separation shock wave is known to be a result of the free interaction of the boundary layer with the outer inviscid flow [16]. Hama showed that the lip separation shock in all cases was due to the viscous separation effect [24]. The viscous separation effect can be described as the shock formation due to the coalescing of compression waves created by the gradual deflection of the external flow by the boundary layer. Strong viscous–inviscid interactions of this type are often explained using simple free-interaction theory [11,13,16,20]. The free-interaction equation of Chapman [13] for uniform flow is given in (1).

$$\frac{p\left(\bar{x}\right)-p\left(\bar{x}_{\mathrm{o}}\right)}{q_{\mathrm{o}}}=F\left(\bar{x}\right)\left[\frac{2C_{f_{\mathrm{o}}}}{\sqrt{M_{\mathrm{e,o}}^{2}-1}}\right]^{0.5} \tag{1}$$

where

$$F\left(\bar{x}\right)=\left[f_{1}\left(\bar{x}\right)f_{2}\left(\bar{x}\right)\right]^{0.5} \tag{2}$$

Here, $\bar{x}$ is the normalized distance along the wall. The pressure distribution and C_{fo} are taken at the wall. $M_{\mathrm{e,o}}$ and

q_o are properties at the boundary layer edge at the interaction onset. The function $f_1(\bar{x}) = \int_{\bar{x}_o}^{\bar{x}} \left(\frac{\partial \bar{\tau}}{\partial \bar{y}}\right)_w d\bar{x}$ represents the integral in the streamwise direction of the shear stress term in the boundary layer equation at the wall. The function $f_2(\bar{x})$ is the non-dimensional streamline deflection due to viscous–inviscid interaction. $F(\bar{x})$ is a correlation parameter between the properties at the interaction onset and the separation pressure rise. This parameter has been found to be nearly Reynolds number independent in uniform flow. Equation 1 was successfully used by Erdos and Pallone [20] to model the pressure rise through a separation interaction.

Free-interaction theory was first extended to non-uniform flow by Carrière et al. [11] who presented a generalized theory for non-uniform flow in a pressure gradient p'. This is shown in (3).

$$F\left(\bar{x}, p'\right) = \sqrt{\left(\frac{P - P_o}{q_o}\right)\left(\frac{\bar{\nu}(\bar{x}) - \nu(\bar{x})}{\sqrt{C_{f_o}}}\right)} \tag{3}$$

Here $\bar{\nu}$ and ν are the Prandtl–Meyer functions for unseparated flow and separated flow, respectively. p' is the non-dimensional pressure gradient due to non-uniformity. By including the difference in the Prandtl–Meyer function in this manner, the effect of the non-uniformity is accounted for. Both $F(\bar{x})$ and $F\left(\bar{x}, p'\right)$ have been useful as predictive equations based on empirical data [11,20]. Non-uniform free-interaction theory has received renewed attention recently for understanding and modeling of shock wave boundary layer interactions in nozzles [1,10,29,37]. In the present work, the primary goal is to derive an equation that is more useful to the near-wake separation problem and can be more readily used with CFD or experimental data to provide insight into the physics.

Equation 3 is useful and could be applied to an aft-body assuming that the Prandtl–Meyer function $\bar{\nu}(\bar{x})$ along the external streamline in attached flow is known. This would require a separate simulation or experiment of unseparated flow and is less convenient than using the CFD data or experimental data alone. Additionally, in the case of an aft-body there is always separation, thus making this approach less feasible. In the present study we derive a different free-interaction equation by applying the same assumptions as Carrière et al. [11] but through a different process. Here, the total streamline deflection is written as a linear combination of the streamline deflection due to viscous–inviscid interaction ($\Delta\varphi$) and geometry ($\Delta\alpha$). A possible improvement for future work would be to separate the deflection due to viscous–inviscid interaction ($\Delta\varphi$) into a sum of the deflection due to the attached boundary layer growth and the separation growth as done by Carrière et al. [11]. By following the derivation process outlined by Délery [16] for the Chapman [13] free-interaction theory, an equation in the same form as (1) results. The resulting free-interaction equation is given in (4) and (5). The full derivation is given in the Appendix.

$$\frac{p(\bar{x}) - p(\bar{x}_o)}{q_o} = F^*(\bar{x}) \sqrt{\frac{2C_{fo}}{\left(M_{e,o}^2 - 1\right)^{1/2}}} \tag{4}$$

where

$$F^*(\bar{x}) = \left[f_1(\bar{x})\, f_2(\bar{x}) + \frac{L_{sep}^2}{\delta_o^* r} f_1(\bar{x})\, f_3(\bar{x}) \right]^{0.5} \tag{5}$$

Certain parameters that disappear in the uniform flow derivation remain and must be known. In the present work, the onset of the interaction is assumed to be located in close proximity to the pressure minimum. The properties at this location are given the subscript ($_o$). δ_o^* is calculated by examining the velocity profile in the direction normal to the surface at the location of the pressure minimum. L_{sep} is taken as the distance between the pressure minimum and the separation location. The function $f_2(\bar{x})$ is the non-dimensional effective streamline deflection due to viscous–inviscid interaction. In general this function can accurately be assumed to be $f_2(\bar{x}) = \frac{d\bar{\delta}^*}{d\bar{x}}$. However, in the present case where the normal pressure gradient is non-zero we have elected to not explicitly identify this term. Instead it is represented as $f_2(\bar{x}) = \Delta\varphi_{eff}$. In contrast to Carrière et al. [11], here $\Delta\varphi_{eff}$ represents the effective total streamline deflection due to viscous–inviscid interaction. The third parameter, $f_3(\bar{x}) = \Delta\bar{\alpha}$, is the dimensionless angle change due to cylinder surface curvature. This equation is derived for a cylinder, but would also be appropriate for a different geometry provided the radius of curvature (r) is relatively constant through the interaction region.

The function $F^*(\bar{x})$ is a correlation parameter between the pressure rise in the interaction, and the properties at interaction onset. Unlike the definition of the free-interaction parameters $F(\bar{x})$ or $F'\left(\bar{x}, p'\right)$, $F^*(\bar{x})$ includes the effect of the viscous–inviscid interaction as well as the curvature of the aft-body. Thus their contributions to the total pressure rise can be examined separately. It can be observed from (5) that the term representing the effect of curvature ($\frac{L_{sep}^2}{\delta_o^* r} f_1(\bar{x})\, f_3(\bar{x})$) is dependent on the length of separation. Thus, we can see that interactions occurring over a smaller curve length have less dependence on curvature and vice-versa. Similarly, in interactions where there is no curvature ($f_3(\bar{x}) = 0$) there is no dependence on separation length [i.e., $F^*(\bar{x}) = F(\bar{x})$].

Like Carrière et al. [11], in the present study we are particularly interested in the viscous–inviscid free-interaction mechanism. Therefore it is desirable to subtract the effect of surface deflection on the interaction parameter to recover the classical free-interaction parameter $F(\bar{x}) = \sqrt{f_1(\bar{x})\, f_2(\bar{x})}$. This parameter can be calculated by rearranging (4) to give

(6). This is derived in the Appendix.

$$F(\bar{x}) = \sqrt{f_1(\bar{x})\, f_2(\bar{x})} = \left[\left(\frac{p(\bar{x}) - p(\bar{x}_o)}{q_o} \right)^2 \frac{\sqrt{M_{e,o}^2 - 1}}{2C_{f_o}} - \frac{L_{sep}^2}{\delta_o^* r} f_1(\bar{x})\, f_3(\bar{x}) \right]^{0.5} \quad (6)$$

The resulting free interaction parameter, rather than being a function of Prandtl–Meyer functions, is a function of the boundary layer properties through the interaction region. Additionally, it is a correlation between the fraction of the pressure rise due to viscous–inviscid interaction and the properties at interaction onset, not the overall pressure rise. In order to use the above equation, an accurate estimate or measurement of the surface normal gradient in shear-stress through the interaction region is required. The parameter $f_1(\bar{x})$ can be explicitly calculated from the simulation results using the viscous stress tensor τ and (7).

$$f_1(\bar{x}) = \frac{\delta_o^*}{|\tau_{wo}|} \int_{\bar{x}_o}^{\bar{x}} (\nabla \cdot \tau) \cdot \hat{t}\, d\bar{x} \quad (7)$$

3 Simulation details

3.1 Solver and setup

The open source CFD software, OpenFOAM v.2.2.1, with the solver, rhoCentralFoam, was used to simulate the problem. The flow is assumed to be laminar, in equilibrium, and a continuum. The gas is treated as an ideal gas. The solver rhoCentralFoam is a density-based solver of the unsteady, compressible Navier–Stokes equations as shown in (8)–(10) [23].

$$\frac{\partial \rho}{\partial t} + \nabla \cdot (\rho u) = 0 \quad (8)$$

$$\frac{\partial (\rho u)}{\partial t} + \nabla \cdot (\rho u^2) - \nabla p - \nabla \cdot \tau = 0 \quad (9)$$

$$\frac{\partial \rho E}{\partial t} + \nabla \cdot (u(\rho E)) + \nabla \cdot [up] + \nabla \cdot (\tau \cdot u) + \nabla \cdot j = 0, \quad (10)$$

where ρ, u, p, j, τ, and E represent the density, velocity, pressure, diffusive heat flux, viscous stress tensor, and total energy density, respectively. This solver has been used successfully to model hypersonic flow problems with strong shock waves [3–5,23].

3.2 Boundary conditions and geometry

Simulations were performed at approximately Mach 5.9 over a range of free-stream Reynolds numbers (8×10^3 to 8×10^4). The cylinder diameter (0.032 m) was used as the characteristic length scale. Mach number was fixed at the inlet by specifying a constant static temperature (158 K) and velocity (1552 m/s). Reynolds number was then fixed with inlet pressure. Simulations were performed with, and without, the no-slip condition at the wall. The mesh was generated using the native OpenFOAM meshing utility, blockMesh. The geometric setup is shown in Fig. 2. The mesh independent grid consisted approximately 8 million hexahedral elements.

3.3 Gas properties modeling

Characterizing hypersonic flow using similarity parameters such as Mach number and Reynolds number is inherently limited by the dependence on temperature-dependent gas properties. Therefore, any quantitative comparisons made here are gas- and inlet-property specific. General qualitative relationships between parameters should still hold for different gases and inlet conditions. Nitrogen was selected as the working fluid because it has low dissociation below 3000 K, has similar properties to air, and is often used in high-speed wind tunnels. A 7-coefficient NASA thermodynamics relation, based on the NIST-JANAF [34] thermochemical tables was used to model gas thermodynamic properties. The polynomials are given in (11)–(13). Here, a_1–a_7 are coefficients dependent on the particular gas used, c_p is the constant pressure-specific heat capacity, H is the enthalpy, and S is entropy. The polynomial coefficients utilized have been validated against the NIST database from 100 to 6000 K.

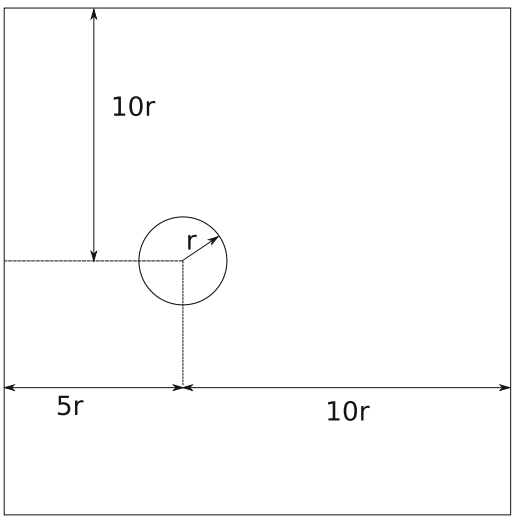

Fig. 2 Simulation domain (not to scale)

$$\frac{c_p}{R} = (a_1 + a_2 T + a_3 T^2 + a_4 T^3 + a_5 T^4) \tag{11}$$

$$\frac{H}{R} = (a_1 T + a_2 T^2/2 + a_3 T^3/3 + a_4 T^4/4 + a_5 T^5/5 + a_6) \tag{12}$$

$$\frac{S}{R} = (a_1 \ln T + a_2 T + a_3 T^2/2 + a_4 T^3/3 + a_5 T^4/4 + a_7) \tag{13}$$

Sutherland's law is used to model the fluid viscosity, and is given in (14). Here μ_o is the reference viscosity, T is the temperature, T_o is the reference temperature and C is the Sutherland constant. The static temperatures of the simulation stay within the acceptable range for the NIST-JANAF polynomials and Sutherland's law [2,39].

$$\mu = \mu_o \frac{T_o + C}{T + C} \left(\frac{T}{T_o}\right)^{3/2} \tag{14}$$

The modified Eucken method given in (15) is used to model the thermal conductivity, κ. Here, c_v is the constant volume-specific heat capacity, and R_g is the specific gas constant.

$$\kappa = \mu c_v \left(1.32 + \frac{1.77 R_g}{c_v}\right) \tag{15}$$

3.4 Assumption of laminar flow

The flow features of interest are assumed to be predominantly laminar for the Reynolds numbers investigated in this work. There is significant uncertainty in this assumption given the highly complicated nature of transition in supersonic free-shear layers. The Reynolds number range was selected based on ranges investigated in comparable studies [22,32]. To increase confidence in this assumption, the highest Reynolds number case ($Re_\infty = 80{,}000$) was found to satisfy the empirical correlation from Lees [30].

4 Simulation results

4.1 Model validation and grid independence

Numerical grid independence was performed at the maximum Reynolds number ($Re_\infty = 8 \times 10^4$) by examining changes in the pressure distribution and separation location. A Richardson extrapolation was used to estimate the uncertainty of the working grid. A 2.7 % difference in pressure distribution, and 0.2° difference (<0.2 % measured from the forward stagnation point) in separation location were found between the mesh-independent grid and the Richardson extrapolated result. The relatively high error in pressure is due to the low pressures on the aft-body. The maximum change in pressure normalized by the post-shock stagnation pressure is 0.07 %. A less dense mesh was used in the slip cases as there was no boundary layer to resolve at the wall.

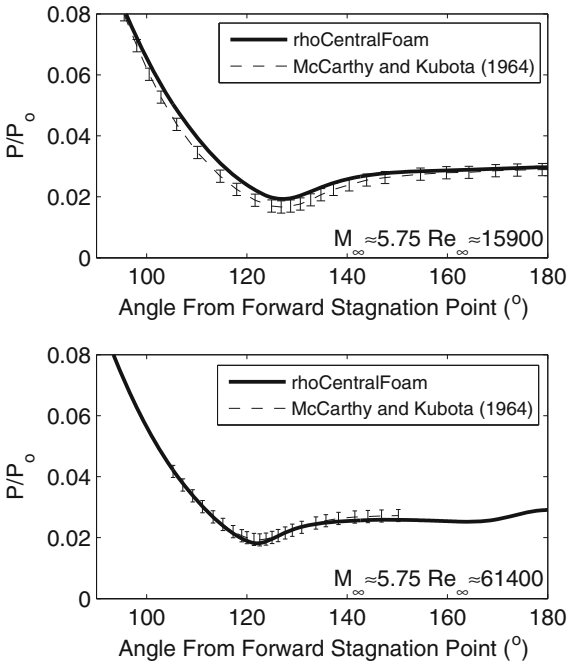

Fig. 3 Comparison of wall pressure distribution to the results of McCarthy and Kubota [32]

The numerical solver and setup were validated by comparison to the experimental data from McCarthy and Kubota [32]. These simulations were used as a first step to ensure the accuracy of the open-source solver (rhoCentralFoam), and to ensure the physics were adequately captured. Figure 3 shows a comparison of the pressure distribution in the base region at two Reynolds numbers. The pressure distribution is known to be a net result of the viscous–inviscid interaction between the boundary layer development and the external inviscid flow. The results of the simulation show reasonable agreement with the experimental data. Some error is present because the free-stream Mach and Reynolds numbers reported by McCarthy and Kubota are approximate or nominal values, and thus may not exactly match the simulated values. Data at different Reynolds numbers were available and showed similar agreement.

4.2 Analysis and discussion

4.2.1 Slip vs. no-slip simulations

The purpose of the comparison of slip and no-slip simulations was given in the introduction. The difference between the slip and no-slip simulations is illustrated in Figs. 4 and 5 at a representative Reynolds number ($Re_\infty = 4 \times 10^4$). Synthetic Schlieren and streamlines are used to clearly show the

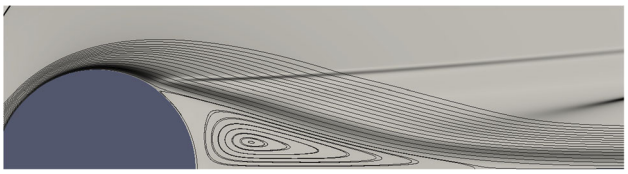

Fig. 4 Flow-field topology for flow with no-slip boundary condition ($Re_\infty = 40{,}000$)

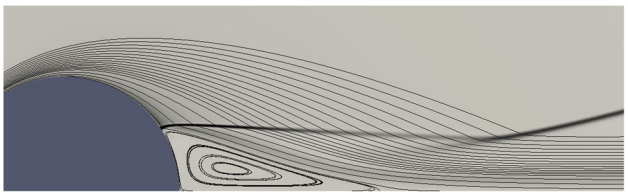

Fig. 5 Flow-field topology for flow with slip boundary condition ($Re_\infty = 40{,}000$)

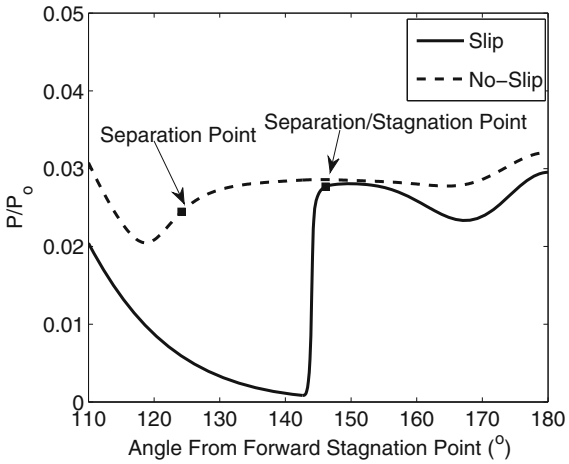

Fig. 6 Pressure distributions through separation region for slip and no-slip boundary ($Re_\infty = 80{,}000$)

important flow features. All of the pertinent flow topology is present despite the absence of a boundary layer on the wall. As expected, the generation of the separated near-wake does not require the presence of a boundary layer and is required due to gas dynamics effects. This can be explained as follows: in order for the flow to remain attached (i.e., no wake), the flow would need to undergo an instantaneous deflection of 90° at the base stagnation point, which is impossible. This abrupt deflection first leads to a shock wave, and the viscous recirculation region is formed after. This is why the slip simulations are an appropriate simplified analog to the fully viscous near-wake simulations.

The pressure distributions for the slip and no-slip cases are examined in Figs. 6, 7 and 8. The pressure distribution through the separation region is shown for the slip and no-slip cases at the same free-stream Reynolds numbers. The separation point is marked for both cases. The point of flow reversal occurs at the peak of the pressure rise in the slip case because there is no stagnation pressure deficit due to a boundary layer. In the no-slip case, the interaction is spread over a length of a few boundary layer thicknesses on the body. This is also visible in the synthetic Schlieren images in Figs. 4 and 5. The dip in pressure along the base visible in Figs. 6, 7 and 8 is due to the regions of localized compression and expansion noted by Grasso et al. [22]. We can see that all of the pertinent flow features are present in the slip simulations and thus we have successfully created a scenario where the off-body viscous effects are isolated from the viscous effects in the boundary layer.

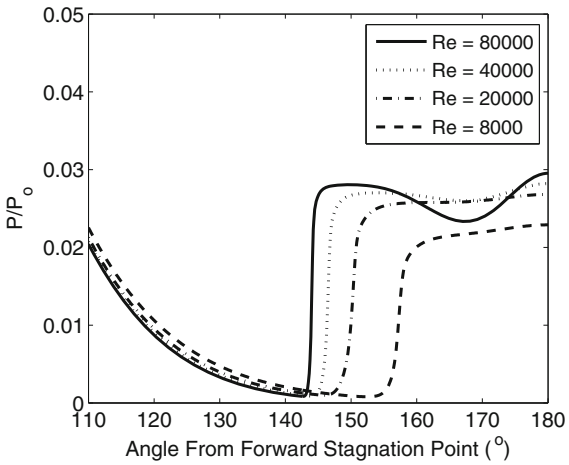

Fig. 7 Pressure distributions through the separation region at various free-stream Reynolds numbers—slip case

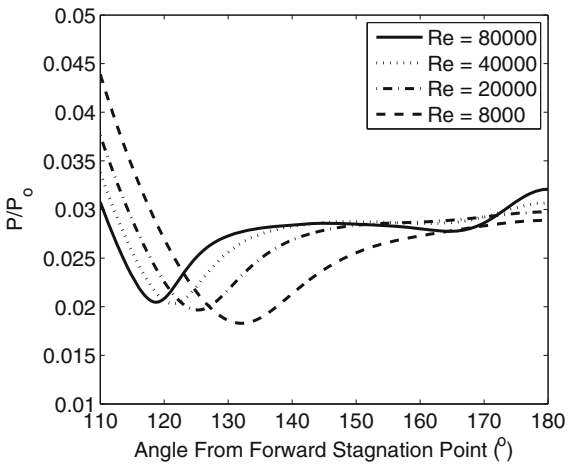

Fig. 8 Pressure distributions through the separation region at various free-stream Reynolds numbers—no-slip case

4.2.2 Strong interaction onset

The location of the strong-interaction is important for determining the size of the near-wake and the lip separation shock location. In the case here where the wall has a slip condition,

but the ratio of viscous and inertial forces in the external flow is still manipulated, the jump location should still be a function of the Reynolds number. The only mechanisms that can act to alter the location of this jump in the slip case is the subsonic region downstream in the near-wake and the off-body viscous forces. If there were no Reynolds number dependence, the jump would be fixed and would indicate a purely inviscid mechanism. Through comparison of the slip and no-slip cases, it is observed that the pressure minimum moves with a similar direction and magnitude in both cases in response to an increase in Reynolds number (Figs. 7, 8). This leads to the conclusion that the dominant mechanism to move separation upstream is the same in both cases. The overall location of the interaction onset is determined by the balance between the upstream and the near-wake forces. The relative displacement of the interaction onset location for a given geometry in response to a change in Reynolds is predominantly due to a change in the ratio of viscous to inertial forces in the wake.

4.2.3 Shoulder expansion and weak viscous–inviscid interaction

The importance of the shoulder expansion to the formation of the lip shock has been documented by Hama [24] as well as Weiss and Weinbaum [44–47]. This is most often referring to the rate of expansion that is dependent on the shoulder geometry. A less explored effect in the expansion region is the Reynolds number dependence that arises due to weak-viscous–inviscid interaction on geometries with gradual shoulder expansions. For example, in the present case of the cylinder the shoulder expansion is not sudden. As illustrated in Fig. 1, the flow expanding around the cylinder undergoes a weak interaction between the shear flow and the expansion fan in the external flow near the shoulder. This flow feature is Reynolds number dependent and has not received extensive study regarding its impact on the near-wake. This interaction affects the rate of flow expansion around the body. Because of this effect, the weak interaction will affect the Mach number, pressure, and boundary layer properties at the onset of the strong viscous–inviscid interaction. Figure 9 shows the Mach number at the edge of the viscous layer ($\approx 0.99\,U_e$) as a function of the angle from the forward stagnation point. As the Reynolds number is decreased, the weak-interaction between the shear flow on the body and the external flow becomes more significant and therefore the flow expands less. It is known that a higher expansion, in general, should result in a stronger lip shock wave. Thus it would appear that the Reynolds number effect on the shoulder expansion will in turn affect the strength of the lip shock. However, the rate of expansion is still primarily a geometric effect and thus the relative importance of the weak interaction will depend on the geometry.

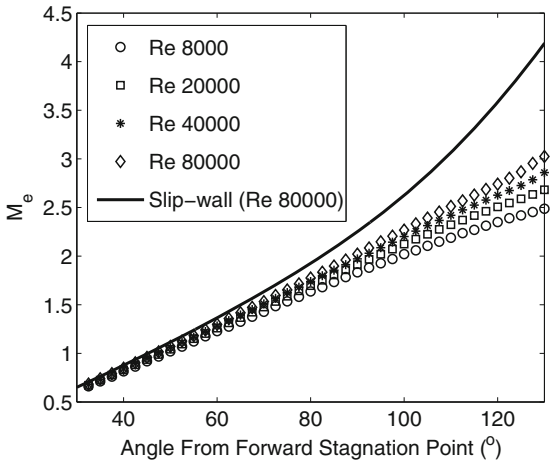

Fig. 9 External Mach number M_e vs. angle from forward stagnation point (°)

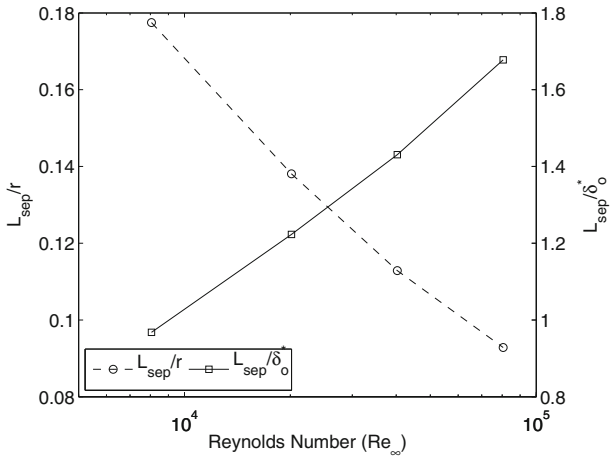

Fig. 10 Separation length vs. Reynolds number

4.2.4 Separation shock and the strong viscous–inviscid interaction

The formation of the lip separation shock is analyzed here using the free-interaction theory discussed in Sect. 2. It was noted that the separation length is fundamentally important to the effect of curvature on the free-interaction. In Fig. 10 the separation length is shown vs. free-stream Reynolds number. These curves show the expected relationship of L_{sep}/δ_o and L_{sep}/r with increasing Reynolds number. As the Reynolds number is decreased, the separation length normalized by cylinder radius (L_{sep}/r) increases. The opposite is true for separation length normalized by displacement thickness (L_{sep}/δ_o^*). The product of these two parameters is the coefficient of the curvature term and increases with Reynolds number. Therefore the simulation results have shown that the importance of the surface curvature to the overall free-interaction decreases with increasing Reynolds number.

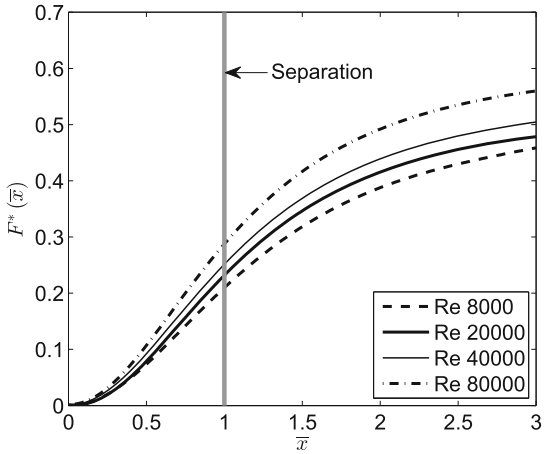

Fig. 11 $F^*(\bar{x})$ profiles at various Reynolds numbers

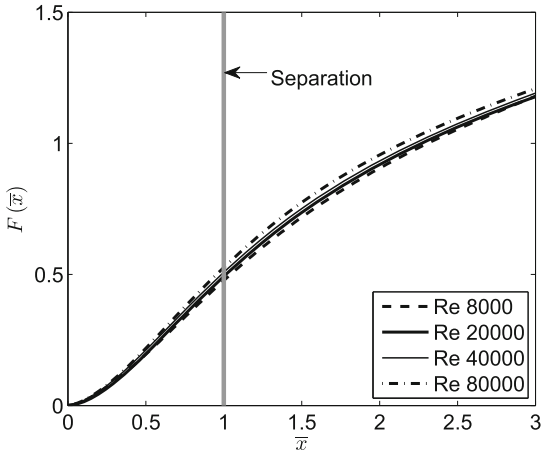

Fig. 12 $F(\bar{x})$ profiles at various Reynolds numbers

Figure 11 shows the parameter $F^*(\bar{x})$ at various Reynolds numbers calculated using wall pressure gradient and the properties at the interaction onset. It is clear that without correcting for the effect of the surface curvature there is a significant Reynolds number dependence. By examining (4) we can see that the implications of this observation are that two flows with the same Mach number and shear stress will result in a different profile of dimensionless shock strength on a body of curvature. However, this only indicates that the overall interaction is Reynolds number dependent and does not address the question of similarity of the underlying viscous–inviscid interaction mechanism.

Figure 12 shows the interaction parameter $F(\bar{x})$ calculated from simulation data using (6) and (7). The curves nearly collapse onto a single profile over an order of magnitude increase in Reynolds number. Thus we can make the conclusion that like the free-interactions at separation in classical SWBLI, this component of the free-interactions leading to laminar near-wake separation obey a similarity that is mostly Reynolds number independent. This fraction of the overall pressure rise leading to the lip separation shock is Reynolds number independent. We can further conclude that the Reynolds number dependence seen in the parameter $F^*(\bar{x})$ is a consequence of the interaction occurring over a finite length on a body of curvature.

From Fig. 12, at separation ($\bar{x} = 1$) the value of the interaction parameter is nearly constant (≈0.5). This is noticeably lower than those for a regular shock wave boundary layer interaction in laminar flow (≈0.8 for general SWBLI). A likely reason for the lower-strength interaction in these flows is that the boundary layer on the aft-body has less momentum close to the wall compared to a flat plate. A similar justification is often used for the increased value of this parameter in turbulent flow. A small Reynolds number dependence is still seen in $F(\bar{x})$ after the correction for surface curvature. This dependence could be due to the assumption that the compression can be approximated by an effective linearized isentropic compression occurring at the external inviscid streamline, or the neglected unseparated boundary layer growth (as accounted for by Carrière et al.). Additionally, the flow has a non-zero normal pressure gradient, and remains rotational away from the wall as was discussed by Weiss and Weinbaum [47]. The non-similar nature of the flow and the Reynolds number dependence of the weak viscous–inviscid interaction on the forebody may also contribute to this remaining dependence.

4.2.5 Analysis summary

By examining (4) and (5), we can form a summary regarding the origin of the Reynolds number dependence in the strong interaction leading to the lip separation shock. The part of the viscous–inviscid interaction represented by the term $f_1(\bar{x})\, f_2(\bar{x})$ has been shown here to be mostly Reynolds number independent. The term representing the effect of curvature ($\frac{L_{\text{sep}}^2}{\delta_o^* r} f_1(\bar{x})\, f_3(\bar{x})$) decreases the strength of the pressure rise at separation with decreasing Reynolds number. The remaining variables are C_{f_o} and $M_{e,o}$. The value of these variables are determined by the combined effect of the weak-interaction, and the off-body viscous forces in the near-wake. This effect determines the distribution of C_f and M_e along the body and the location of the interaction onset x_o (shown using the slip-simulations). Through this process we have isolated and further explained the underlying Reynolds number dependencies of the aft-body strong interaction leading to the formation of the lip shock.

5 Conclusion

Flow over an adiabatic circular cylinder was simulated over a range of Reynolds numbers at a free-stream Mach number of

5.9. Simulation results showed close agreement with experimental wall-pressure distributions. Slip simulations were performed to create a limiting scenario where a near-wake is formed in the absence of a boundary layer. A comparison of slip and no-slip simulations was performed in order to isolate the off-body viscous effects in the near-wake. A similar Reynolds number dependence of the onset location of strong interaction was present in both cases. This demonstrated that the off-body viscous effects play a dominant role in the relative displacement of the interaction onset location due to a change in Reynolds number for a given geometry. A free-interaction equation and a correlation parameter $F^*(\bar{x})$ were presented specifically for the strong (lip-shock) interaction on a cylindrical aft-body. It was shown using this correlation parameter that the effect of curvature on the lip-shock formation is dependent on the Reynolds number. It was shown that the free-interaction parameter $F(\bar{x})$ could be recovered algebraically from $F^*(\bar{x})$ to isolate the component of the pressure rise due to the viscous–inviscid interaction. Using this it was shown that the profile of $F(\bar{x})$ (and therefore its effect on the overall strong interaction) is Reynolds number independent. Additionally, the value of $F(\bar{x})$ at separation was lower than that of a general shock wave boundary layer interaction. These observations were then combined with an examination of the free-interaction equation derived. The result was a thorough analysis of the Reynolds number dependence of the separation process and subsequent pressure rise leading to the lip shock.

Acknowledgments This research was enabled in part by support provided by WestGrid (http://www.westgrid.ca) and Compute Canada Calcul Canada (http://www.computecanada.ca). Financial support was provided by Dr. Johansen's Discovery Grant under the Natural Sciences and Engineering Research Council of Canada (NSERC). Mr. Hinman was partially supported through the Queen Elizabeth II Graduate Scholarship (QEII) administered by the government of Alberta.

Appendix: Derivation of free-interaction for a cylindrical aft-body

The following derivation follows closely the derivation given by Délery [16] for the Chapman [13] free-interaction theory. Starting with the boundary layer momentum equation in the streamwise direction at the wall the following simple relationship can be found. In these derivations, x refers to the streamwise distance, and y refers to the wall normal distance.

$$\frac{\mathrm{d}p}{\mathrm{d}x} = \left(\frac{\partial \tau}{\partial y}\right)_{\mathrm{w}} \tag{16}$$

Integrating both sides:

$$p(\bar{x}) - p(\bar{x}_{\mathrm{o}}) = \int_{x_{\mathrm{o}}}^{x} \left(\frac{\partial \tau}{\partial y}\right)_{\mathrm{w}} \mathrm{d}x \tag{17}$$

Introducing the non-dimensional variables $\bar{\tau} = \tau/\tau_{\mathrm{wo}}$, $\bar{y} = y/\delta^*_{\mathrm{o}}, q_{\mathrm{o}} = 0.5\gamma p_{\mathrm{e}}(x_{\mathrm{o}}) M^2_{\mathrm{e,o}}$ and $C_{fo} = \tau_{\mathrm{wo}}/q_{\mathrm{o}}$ the equation becomes:

$$\frac{p(\bar{x}) - p(\bar{x}_{\mathrm{o}})}{q_{\mathrm{o}}} = C_{fo}\frac{L_{\mathrm{sep}}}{\delta^*_{\mathrm{o}}} f_1(\bar{x}) \tag{18}$$

where:

$$f_1(\bar{x}) = \int_{\bar{x}_{\mathrm{o}}}^{\bar{x}} \left(\frac{\partial \bar{\tau}}{\partial \bar{y}}\right)_{\mathrm{w}} \mathrm{d}\bar{x} \tag{19}$$

This is the first equation needed to define the interaction. The second equation represents the pressure rise due to external flow deflection.

$$\frac{\sqrt{M^2_{\mathrm{e,o}} - 1}}{\gamma M^2_{\mathrm{e,o}}}\frac{\mathrm{d}p}{p} = \mathrm{d}\varphi \tag{20}$$

In its linearized form:

$$\frac{\sqrt{M^2_{\mathrm{e,o}} - 1}}{\gamma M^2_{\mathrm{e,o}}}\frac{\Delta p}{p} = \Delta\varphi \tag{21}$$

The following is the only significant difference from the derivation of Chapman [13,16]. The streamline deflection angle φ in the case of a cylinder is the sum of the deflection from viscous–inviscid interaction and the deflection of the cylindrical aft-body. As well, because we know that there is vertical pressure gradient and rotational flow, the deflection is actually an effective angle that would result in the given pressure rise. In the general case of flat-plate flow it is a good assumption that the compression is only due the displacement thickness growth $\mathrm{d}\delta^*/\mathrm{d}x$. Here we do not specify that this is the specific viscous–inviscid mechanism. Therefore:

$$\frac{\sqrt{M^2_{\mathrm{e,o}} - 1}}{\gamma M^2_{\mathrm{e,o}}}\frac{\Delta p}{p} = \Delta\varphi_{\mathrm{eff}} + \Delta\alpha, \tag{22}$$

where $\Delta\varphi_{\mathrm{eff}}$ is the effective angle change due to viscous–inviscid interaction. $\Delta\alpha$ is the angle change due to the surface deflection of the cylinder. If we assume that $\Delta\varphi_{\mathrm{eff}}$ scales with $\delta^*_{\mathrm{o}}/L_{\mathrm{sep}}$, and $\Delta\alpha$ scales with the angular length of the interaction $\theta_{\mathrm{sep}} = L_{\mathrm{sep}}/r$ and introducing the same dimensionless variables as the previous step, we can get the following function:

$$\frac{p(\bar{x}) - p(\bar{x}_{\mathrm{o}})}{q_{\mathrm{o}}} = \frac{2}{\sqrt{M^2_{\mathrm{e,o}} - 1}}\left[\frac{\delta^*_{\mathrm{o}}}{L_{\mathrm{sep}}} f_2(\bar{x}) + \theta_{\mathrm{sep}} f_3(\bar{x})\right] \tag{23}$$

The function $f_2(\bar{x})$ is the dimensionless effective angle change due to viscous–inviscid interaction. In the flat-plate case this can be assumed to be equal to $\mathrm{d}\bar{\delta}^*_\mathrm{o}/\mathrm{d}\bar{x}$. The function $f_3(\bar{x})$ is the dimensionless angle change due to the cylinder angle. Multiplying (18) and (23) and taking the square root we get the following:

$$\frac{p(\bar{x}) - p(\bar{x}_\mathrm{o})}{q_\mathrm{o}} = \sqrt{\frac{2C_{fo}}{\left(M^2_{\mathrm{e,o}} - 1\right)^{1/2}}} \left[f_1(\bar{x})\, f_2(\bar{x}) + \frac{L^2_{\mathrm{sep}}}{\delta^*_\mathrm{o} r} f_1(\bar{x})\, f_3(\bar{x}) \right]^{0.5} \tag{24}$$

or

$$\frac{p(\bar{x}) - p(\bar{x}_\mathrm{o})}{q_\mathrm{o}} = F^*(\bar{x}) \sqrt{\frac{2C_{fo}}{\left(M^2_{\mathrm{e,o}} - 1\right)^{1/2}}} \tag{25}$$

The above equation is in the same form as the free-interaction theory equation from Chapman [13]. However, the interaction parameter is denoted $F^*(\bar{x})$ because it incorporates both the effect of the geometry and the free-interaction. This equation would also be appropriate for a geometry other than a cylinder provided the radius of curvature is relatively constant throughout the interaction region. Equation 24 can be rearranged for the free-interaction parameter $F(\bar{x}) = \sqrt{f_1(\bar{x})\, f_2(\bar{x})}$ to give:

$$F(\bar{x}) = \sqrt{f_1(\bar{x})\, f_2(\bar{x})} = \left[\left(\frac{p(\bar{x}) - p(\bar{x}_\mathrm{o})}{q_\mathrm{o}} \right)^2 \frac{\sqrt{M^2_{\mathrm{e,o}} - 1}}{2C_{fo}} - \frac{L^2_{\mathrm{sep}}}{\delta^*_\mathrm{o} r} f_1(\bar{x})\, f_3(\bar{x}) \right]^{0.5} \tag{26}$$

References

1. Aghababaie, A.A., Theunissen, R.: Modeling free shock separation induced side loads in overexpanded rocket nozzles. AIAA J. **53**(1), 93–103 (2015). doi:10.2514/1.J053014
2. Anderson, J.D.: Hypersonic and High-Temperature Gas Dynamics, 2nd edn. American Institute of Aeronautics and Astronautics, Blacksburg (2006)
3. Arisman, C., Johansen, C.T.: Nitric oxide chemistry effects in hypersonic boundary layers. AIAA J. **53**(12), 3652–3660 (2015)
4. Arisman, C., Johansen, C.T., Bathel, B., Danehy, P.: Investigation of gas seeding for planar laser-induced fluorescence in hypersonic boundary layers. AIAA J. **53**(12), 3637–3651 (2015)
5. Arisman, C., Johansen, C.T., Galuppo, W., McPhail, A.: Nitric oxide chemistry effects in hypersonic boundary layers. In: 43rd Fluid Dynamics Conference. American Institute of Aeronautics and Astronautics, Reston, Virginia (2013). doi:10.2514/6.2013-3104
6. Bashkin, V.A., Vaganov, A.V., Egorov, I.V., Ivanov, D.V., Ignatova, G.A.: Comparison of calculated and experimental data on supersonic flow past a circular cylinder. Fluid Dyn. **37**(3), 473–483 (2002)
7. Baum, E.: Interacting supersonic laminar wake calculations by a finite difference method. AIAA J. **5**(7), 1224–1230 (1967). doi:10.2514/3.4175
8. Baum, E.: An interaction model of a supersonic laminar boundary layer on sharpand rounded backward facing steps. AIAA J. **6**(3), 440–447 (1968). doi:10.2514/3.4518
9. Baum, E., King, H.H., Denison, M.R.: Recent studies of the laminar base-flow region. AIAA J. **2**(9), 1527–1534 (1964)
10. Bekka, N., Sellam, M., Chpoun, A.: Aeroelastic stability analysis of flexible overexpanded rocket nozzle. Shock Waves (2015). doi:10.1007/s00193-015-0575-2
11. Carrière, P., Sirieix, M., Solignac, J.L.: Similarity properties of the laminar or turbulent separation phenomena in a non-uniform supersonic flow. In: Hetenyi, M., Vincenti, W.G. (eds.) Applied Mechanics. Proceedings of the Twelfth International Congress of Applied Mechanics, Stanford University, August 26–31, 1968 pp. 145–157. Springer, Berlin, Heidelberg (1968)
12. Chapman, D.R.: Laminar mixing of a compressible fluid (Report 958). Technical report, National Advisory Committee for Aeronautics (1950). http://ntrs.nasa.gov/archive/nasa/casi.ntrs.nasa.gov/19930092022.pdf
13. Chapman, D.R., Kuehn, D.M., Larson, H.K.: Investigation of separated flows in supersonic and subsonic streams with emphasis on the effect of transition (Report 1356). Technical report, National Advisory Committee for Aeronautics (1958)
14. Combs, C.S., Clemens, N.T., Danehy, P.M., Bathel, B., Parker, R., Wadhams, T., Holden, M., Kirk, B.: NO PLIF visualization of the orion capsule in LENS-I. In: 51st AIAA Aerospace Sciences Meeting. American Institute of Aeronautics and Astronautics, Grapevine, Texas (2013)
15. Crocco, L., Lees, L.: A mixing theory for the interaction between dissipative flows and nearly isentropic streams. J. Aeronaut. Sci. **19**(10), 649–676 (1952)
16. Delery, J.: Physical introduction, chap. 2. In: Babinsky, H., Harvey, J.K. (eds.) Shock Wave-Boundary Layer Interactions, 1st edn, pp. 5–86. Cambridge University Press, New York (2011)
17. Denison, M.R., Baum, E.: Compressible free shear layer with finite initial thickness. AIAA J. **1**(2), 342–349 (1963). doi:10.2514/3.1535
18. Dewey, C.F.: Near wake of a blunt body at hypersonic speeds. AIAA J. **3**(6), 1001–1010 (1965)
19. Dyakonov, A.A., Schoenenberger, M., Scallion, W.I., Norman, J.W.V., Novak, L.A., Tang, C.Y.: Aerodynamic interference due to MSL reaction control system. In: 41st AIAA Thermophysics Conference, pp. 1–16 (2009)
20. Erdos, J., Pallone, A.: Shock boundry layer interaction and flow separation. In: Proceedings of the 1962 Heat Transfer and Fluid Mechanics Institute, Stanford University Press (1962)
21. Grange, Jm, Klineberg, J.M., Lees, L.: Laminar boundary-layer separation and near-wake flow for a smooth blunt body at supersonic and hypersonic speeds. AIAA J. **5**(6), 1089–1096 (1967)
22. Grasso, F., Pettinelli, C.: Analysis of laminar near-wake hypersonic flows. J. Spacecr. Rockets **32**(6), 970–980 (1995). doi:10.2514/3.26717
23. Greenshields, C.J., Weller, H.G., Gasparini, L., Reese, J.M.: Implementation of semi-discrete, non-staggered central schemes in a colocated, polyhedral, finite volume framework, for high-speed viscous flows. Int. J. Numer. Methods Fluids (2009). doi:10.1002/fld.2069
24. Hama, F.R.: Experimental studies on the lip shock. AIAA J. **6**(2), 212–219 (1968)
25. Hollis, B.R.: Blunt-body entry vehicle aerotherodynamics: transition and turbulent heating. J. Spacecr. Rockets **49**(3), 435–449 (2012). doi:10.2514/1.51864

26. Hruschka, R., O'Byrne, S., Kleine, H.: Comparison of velocity and temperature measurements with simulations in a hypersonic wake flow. Exp. Fluids **51**(2), 407–421 (2011). doi:10.1007/s00348-011-1039-9
27. Johansen, C.T., Danehy, P.M., Ashcraft, S.W., Bathel, B.F., Inman, Ja, Jones, S.B.: Planar laser-induced fluorescence of Mars Science Laboratory reaction control system jets. J. Spacecr. Rockets **50**(4), 781–792 (2013). doi:10.2514/1.A32214
28. Johansen, C.T., Novak, L., Bathel, B.F., Ashcraft, S.W., Danehy, P.M.: Mars Science Laboratory reaction control system jet computations with visualization and velocimetry. J. Spacecr. Rockets **50**(6), 1183–1195 (2013). doi:10.2514/1.A32496
29. Keanini, R.G., Brown, A.M.: Scale analysis and experimental observations of shock-induced turbulent boundary layer separation in nozzles. Eur. J. Mech. B/Fluids **26**(4), 494–510 (2007). doi:10.1016/j.euromechflu.2006.10.002
30. Lees, L.: Hypersonic wakes and trails. AIAA J. **2**(3), 417–428 (1964)
31. Lees, L., Reeves, B.L.: Supersonic separated and reattaching laminar flows: I. General theory and application to adiabatic boundary-layer/shock-wave interactions. AIAA J. **2**(11), 1907–1920 (1964)
32. McCarthy, J.F., Kubota, T.: A study of wakes behind a circular cylinder at m equal 5.7. AIAA J. **2**(4), 629–636 (1964). doi:10.2514/3.2399
33. Nance, R.P., Hollis, B.R., Horvath, T.J., Alter, S.J., Hassan, H.A.: Computational study of hypersonic transitional wake flow. J. Thermophys. Heat Transf. **13**(2), 236–242 (1999). doi:10.2514/2.6441
34. NIST-JANAF: NIST-JANAF Thermochemical Tables (2013). http://kinetics.nist.gov/janaf/
35. O'Byrne, S.: Hypersonic laminar boundary layers and near-wake flows. Ph.D. thesis, The Australian National University (2001)
36. Ohrenberger, J.T., Baum, E.: A theoretical model of the near wake of a slender body in supersonic flow. AIAA J. **10**(9), 1165–1172 (1972). doi:10.2514/3.50344
37. Ostlund, J., Muhammad-Klingmann, B.: Supersonic flow separation with application to rocket engine nozzles. Appl. Mech. Rev. **58**(3), 143 (2005). doi:10.1115/1.1894402
38. Park, G., Gai, S.L., Neely, A.J.: Laminar near wake of a circular cylinder at hypersonic speeds. AIAA J. **48**(1), 236–248 (2010). doi:10.2514/1.44167
39. Rathakrishnan, E.: Theoretical Aerodynamics, 1st edn. John Wiley & Sons Singapore Pte. Ltd., Singapore (2013)
40. Reeves, B.L., Lees, L.: Theory of laminar near wake of blunt bodies in hypersonic flow. AIAA J. **3**(11), 2061–2074 (1965)
41. Skurin, I., Yurkov, A.V.: Approximate calculation of parameters at the throat of a hypersonic wake. J. Appl. Mech. Tech. Phys. **19**(2), 183–187 (1978)
42. Smith, J.H., Lamb, J.P.: Eclectic merger of crocco-lees and chapman-korst approach to near-wake. Int. J. Heat Mass Transf. **17**, 1571–1589 (1974)
43. Tewfik, O.K., Giedt, W.H.: Heat transfer, recovery factor and pressure distributions around a circular cylinder normal to a supersonic rarefied-air stream. J. Aerosp. Sci. **27**(10), 721–729 (1960)
44. Weinbaum, S.: Rapid expansion of a supersonic boundary layer and its application to the near wake. AIAA J. **4**(2), 217–226 (1966). doi:10.2514/3.3422
45. Weiss, R.F.: Base pressure of slender bodies in laminar, hypersonic flow. AIAA J. **4**(9), 1557–1559 (1966). doi:10.2514/3.3735
46. Weiss, R.F.: A new theoretical solution of the laminar, hypersonic near wake. AIAA J. **5**(12), 2142–2149 (1967). doi:10.2514/3.4399
47. Weiss, R.F., Weinbaum, S.: Hypersonic boundary-layer separation and the base flow problem. AIAA J. **4**(8), 1321–1330 (1966). doi:10.2514/3.3672